

RESEARCH ARTICLE | OCTOBER 05 2023

## High-mass metal ion irradiation enables growth of high-entropy sublattice nitride thin films from elemental targets <sup>EP</sup>

Special Collection: [Celebrating the Achievements and Life of Joe Greene](#)

Vladyslav Rogoz <sup>ID</sup>; Oleksandr Pshyk <sup>ID</sup>; Bartosz Wicher <sup>ID</sup>; Justinas Palisaitis <sup>ID</sup>; Jun Lu; Daniel Primetzhofer <sup>ID</sup>; Ivan Petrov <sup>ID</sup>; Lars Hultman <sup>ID</sup>; Grzegorz Greczynski <sup>ID</sup>



*J. Vac. Sci. Technol. A* 41, 063108 (2023)

<https://doi.org/10.1116/6.0003065>



View  
Online



Export  
Citation

CrossMark



**HIDEN**  
ANALYTICAL

## Instruments for Advanced Science

■ Knowledge  
■ Experience ■ Expertise

[Click to view our product catalogue](#)

Contact Hiden Analytical for further details:  
[www.HidenAnalytical.com](http://www.HidenAnalytical.com)  
[info@hiden.co.uk](mailto:info@hiden.co.uk)

**Gas Analysis**



- ▶ dynamic measurement of reaction gas streams
- ▶ catalysis and thermal analysis
- ▶ molecular beam studies
- ▶ dissolved species probes
- ▶ fermentation, environmental and ecological studies

**Surface Science**



- ▶ UHV/TPD
- ▶ SIMS
- ▶ end point detection in ion beam etch
- ▶ elemental imaging - surface mapping

**Plasma Diagnostics**



- ▶ plasma source characterization
- ▶ etch and deposition process reaction kinetic studies
- ▶ analysis of neutral and radical species

**Vacuum Analysis**



- ▶ partial pressure measurement and control of process gases
- ▶ reactive sputter process control
- ▶ vacuum diagnostics
- ▶ vacuum coating process monitoring

# High-mass metal ion irradiation enables growth of high-entropy sublattice nitride thin films from elemental targets

Cite as: J. Vac. Sci. Technol. A 41, 063108 (2023); doi: 10.1116/6.0003065

Submitted: 15 August 2023 · Accepted: 13 September 2023 ·

Published Online: 5 October 2023



Vladyslav Rogoz,<sup>1,2,3,a)</sup>  Oleksandr Pshyk,<sup>1,4</sup>  Bartosz Wicher,<sup>1,5</sup>  Justinas Palisaitis,<sup>1</sup>  Jun Lu,<sup>1</sup>  
Daniel Primetzhofer,<sup>6</sup>  Ivan Petrov,<sup>1,7</sup>  Lars Hultman,<sup>1</sup>  and Grzegorz Greczynski<sup>1</sup> 

## AFFILIATIONS

<sup>1</sup>Department of Physics, Chemistry and Biology (IFM), Thin Film Physics Division, Linköping University, SE-581 83 Linköping, Sweden

<sup>2</sup>Department of Physics, Chemistry and Biology (IFM), Wallenberg Initiative Materials Science for Sustainability, Thin Film Physics Division, Linköping University, SE-581 83 Linköping, Sweden

<sup>3</sup>Sumy State University, 2, Rymskogo-Korsakova St., 40007 Sumy, Ukraine

<sup>4</sup>Laboratory for Surface Science and Coating Technology, Empa, Swiss Federal Laboratories for Materials Science and Technology, Ueberlandstrasse 129, 8600 Dübendorf, Switzerland

<sup>5</sup>Faculty of Materials Science and Engineering, Warsaw University of Technology, 141 Woloska St., 02-507 Warsaw, Poland

<sup>6</sup>Department of Physics & Astronomy, Uppsala University, SE-751 20 Uppsala, Sweden

<sup>7</sup>Materials Research Laboratory, University of Illinois, Urbana-Champaign, Illinois 61801

**Note:** This paper is part of the Special Topic Collection Celebrating the Achievements and Life of Joe Greene.

**a)Electronic mail:** [vladyslav.rogoz@liu.se](mailto:vladyslav.rogoz@liu.se)

## ABSTRACT

Synthesis of high-entropy sublattice nitride (HESN) coatings by magnetron sputtering is typically done using custom-made alloyed targets with specific elemental compositions. This approach is expensive, requires long delivery times, and offers very limited flexibility to adjust the film composition. Here, we demonstrate a new method to grow HESN films, which relies on elemental targets arranged in the multicathode configuration with substrates rotating during deposition. TiVNbMoWN films are grown at a temperature of  $\sim 520^\circ\text{C}$  using Ti, V, Nb, and Mo targets operating in the direct current magnetron sputtering mode, while the W target, operated by high power impulse magnetron sputtering (HiPIMS), provides a source of heavy ions. The energy of the metal ions  $E_{W^+}$  is controlled in the range from 80 to 620 eV by varying the amplitude of the substrate bias pulses  $V_s$ , synchronized with the metal-ion-rich phase of HiPIMS pulses. We demonstrate that  $W^+$  irradiation provides dynamic recoil mixing of the film-forming components in the near-surface atomic layers. For  $E_{W^+} \geq 320$  eV the multilayer formation phenomena, inherent for this deposition geometry, are suppressed and, hence, compositionally uniform HESN films are obtained, as confirmed by the microstructural and elemental analysis.

© 2023 Author(s). All article content, except where otherwise noted, is licensed under a Creative Commons Attribution (CC BY) license (<http://creativecommons.org/licenses/by/4.0/>). <https://doi.org/10.1116/6.0003065>

## I. INTRODUCTION

Protective thin films capable of withstanding harsh environmental conditions significantly improve the physicomechanical properties of a wide range of tools.<sup>1–6</sup> Layers based on high-entropy alloys (HEAs) of metals<sup>7</sup> and their nitrides<sup>8–11</sup> are among the most recent advances in the field, with a present high research activity.

The scientific interest and industrial perspectives of HEAs are very high due to several characteristic effects such as high-entropy effect (stabilization of the solid solution phase due to high configurational entropy), sluggish diffusion effect (reduced diffusion coefficients compared to pure metals), lattice distortion effect (distortion of the lattice due to the random distribution of atoms), and

16 November 2023 15:31:20

cocktail effect (properties that are not present in any of the alloy components).<sup>12</sup> A combination of these factors increases phase and thermal stability, the rate of diffusion decreases, while the movement of dislocations becomes more difficult.<sup>13</sup> This inhibition of defect migration, in turn, is reflected in the improvement of mechanical and tribological properties.<sup>14,15</sup> At low substrate temperatures  $T_s$ , up to 200 °C, an amorphous or quasicrystalline structure may form, while for  $T_s$  in the range 400–700 °C, HEAs crystallize with the formation of a solid solution based on body-centered-cubic (bcc), face-centered-cubic (fcc), or hexagonal (hex) phases, or their mixtures.<sup>16–18</sup>

A HEA can be strengthened by introducing small atomic size chemical elements such as boron, carbon, oxygen, or nitrogen to create high-entropy sublattice nitride (HESN) in the latter case: single-phase solid solution with the anion sublattice occupied by nonmetal atoms.<sup>19,20</sup> HEA and HESN are typically synthesized by magnetron sputtering using alloyed targets.<sup>21–25</sup> Such targets are custom-made with very specific elemental compositions. The price tags are high, and the delivery times are long. Another important limitation of using alloy targets is the lack of possibility to tune the elemental composition, which is often necessary for reaching a specific property.<sup>26</sup>

To address these issues, we propose a new method, which relies on elemental targets of the selected metals mounted on separate magnetrons in a multicathode sputtering system with rotating substrates, such that the average composition of resulting films can be easily controlled by varying the power to each magnetron. To suppress inherent multilayering, the growing film surface is periodically exposed to the flux of heavy metal ions provided by the target operating in the high power impulse magnetron sputtering (HiPIMS) mode.<sup>27,28</sup> The thickness of the ion mixing zone is determined by the metal ion energy, which is controlled by the amplitude of the negative substrate bias pulses  $V_s$  applied synchronously with metal-ion-rich portions of HiPIMS ion fluxes when substrates are facing the ion source.<sup>29</sup> The qualitative details of collision cascades, such as recoil distribution and the ion penetration depths, are obtained from simulations in the open software environment TRIM.<sup>30</sup> We demonstrate the practical implementation of this method using TiVNbMoWN as a model HESN materials system.

## II. EXPERIMENTAL DETAILS

### A. Film deposition

The depositions are performed in a CemeCon AG CC800/9 magnetron sputtering system. The schematic illustration in Fig. 1 shows the experimental layout for the HiPIMS/DCMS (direct current magnetron sputtering) experiments. Four targets operating in the DCMS mode (Ti, V, Nb, and Mo) and one W target driven in the HiPIMS mode are used.

Elements with different masses and different reactivity to  $N_2$  are selected to demonstrate the method's versatility.  $10 \times 20 \times 0.5 \text{ mm}^3$  Si(001) substrates are cleaned in acetone and isopropanol before mounting at the target-to-substrate distance of 18.5 cm. System base pressure is lower than 0.5 mPa ( $5 \times 10^{-6}$  mbar). Before deposition, the chamber is heated up for 2 h to degas the system and reach the required substrate temperature,  $T_s$ , of  $\sim 520$  °C. To minimize the potential surface chemistry modification, the vacuum chamber was vented after the substrates

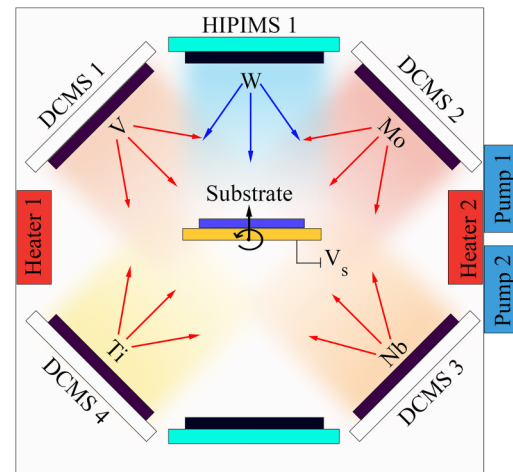


FIG. 1. Top-view schematic illustration of the experimental setup used for film depositions.

had cooled down below 180 °C.<sup>31</sup> The total pressure during sputtering is 0.4 Pa. Depositions are carried out with an  $N_2$ /Ar flow ratio of  $0.18 \pm 0.01$  as regulated by an  $N_2$  feedback loop.<sup>32</sup>

The average HiPIMS and DCMS cathode powers are kept constant at  $P_W = 0.84 \text{ kW}$ ,  $P_{Ti} = 0.2 \text{ kW}$ ,  $P_V = 0.54 \text{ kW}$ ,  $P_{Nb} = 0.23 \text{ kW}$ , and  $P_{Mo} = 0.45 \text{ kW}$  (see Table I). These power values are chosen to obtain the composition of the metal (cation) sublattice close to  $Ti_5V_{21}Nb_5Mo_{34}W_{35}$ , which was predicted by machine learning to have an optimum value of hardness and thermal stability among single-phase HEAs based on common refractory metals (Ti, V, Cr, Zr, Nb, Mo, Hf, W).<sup>33,34</sup>

The HiPIMS pulsing frequency is 200 Hz and the pulse length is set to 30  $\mu\text{s}$ , which provides a target current density  $J_T$  in the range of 1.00–1.04 A/cm<sup>2</sup>. The reported  $J_T$  values can be considered lower limits since they are based on the entire target area (440 cm<sup>2</sup>).

A negative pulsed substrate bias voltage  $V_s$  is applied synchronously with the target pulse.<sup>32,35</sup> 200  $\mu\text{s}$  long bias pulses are applied without the offset with respect to the HiPIMS cathode pulses. Film growth with  $V_s = 60, 300$ , and 600 V is tested to evaluate the effect of bias amplitude (hence, the ion energy and momentum) on the extent of intermixing.

The deposition time is 200 min for films grown with  $V_s = 60 \text{ V}$  and 280 min for layers grown with  $V_s = 300$  and 600 V. The resulting layer thicknesses are in the range 1.3–1.7  $\mu\text{m}$ . The substrate rotation speed was 3.08 rpm.

### B. Characterization techniques

Film thickness and morphology of the films are studied by a ZEISS Sigma 300 scanning electron microscope (SEM) operated with an acceleration voltage of 3 kV and a working distance from 2.3 to 5.3 mm. The elemental compositions were determined by an Oxford Instruments energy dispersive x-ray spectrometer (EDS) coupled to the SEM using Aztec software. Composition depth

16 November 2023 15:31:20

**TABLE I.** Deposition parameters for TiVNbMoWN films.

Composition	Time (s)		$V_s$ , V	Power (W)				
	Total	Per revolution		Ti	V	Nb	Mo	W
Ti <sub>6</sub> V <sub>24</sub> Nb <sub>4</sub> Mo <sub>34</sub> W <sub>32</sub> N	12 000	19.5	60	200	540	230	450	840
Ti <sub>6</sub> V <sub>22</sub> Nb <sub>4</sub> Mo <sub>34</sub> W <sub>34</sub> N	16 800	19.5	300	200	540	230	450	840
Ti <sub>6</sub> V <sub>19</sub> Nb <sub>4</sub> Mo <sub>33</sub> W <sub>38</sub> N	16 800	19.5	600	200	540	230	450	840

profiles were obtained using the time-of-flight elastic recoil detection analysis (ToF-ERDA), employing a 36 MeV  $^{127}\text{I}^{+8}$  primary beam incident at  $67.5^\circ$  to the sample normal and detecting recoils at an angle of  $45^\circ$  with respect to the primary beam.<sup>36</sup> Samples for transmission electron microscopy (TEM) analysis were prepared by employing mechanical thinning, followed by  $\text{Ar}^+$  ion milling until electron transparency. Cross-sectional TEM images and selected area electron diffraction (SAED) patterns were recorded by a FEI Tecnai G<sup>2</sup> TF 20 UT instrument, operated at 200 kV. Scanning TEM (STEM) high-angle annular dark-field (STEM-HAADF) imaging was performed using a Linköping double corrected FEI Titan<sup>3</sup> 60–300, operated at 300 kV. The STEM probe used a 21.5 mrad convergence semiangle, which provided sub-Å resolution with  $\sim 60$  pA beam current. The HAADF-STEM images were recorded using an angular detection range of 46–200 mrad. XRD was performed in Bragg–Brentano configuration with point-focus  $\text{Cu-K}\alpha$  radiation using a Philips X'Pert MRD system.

The Vantage Alpha Nanotester (Micromaterials Ltd., UK) equipped with a Berkovich tip is used to reveal nanoindentation hardness  $H$ . Depth indentations are performed with a constant load of 20 mN during a dwell period of 5 s, resulting in indentation depths <15% of the total film thicknesses. These conditions allow for minimizing elastic behavior from the substrate during the measurements. The reported  $H$  and  $E$  values follow the Oliver and Pharr rule,<sup>37</sup> while the standard deviation errors are extracted from 25 indents (separated by  $40\text{ }\mu\text{m}$  in square grids).

Repeated measurements of reduced Young's modulus were carried out on the thinnest TiVNbMoWN film ( $1.3\text{ }\mu\text{m}$ ) grown with  $V_s = 60$  V. With the maximum load of 30 mN (resulting in an indentation depth of  $\sim 19\%$  of the film thicknesses), the reduced Young modulus was  $319.7 \pm 4.0$  GPa. If a load of 20 mN was used instead (resulting in the indentation depth equal to 15% of the film thickness), the reduced Young's modulus was  $311.7 \pm 5.7$  GPa, which is the same result (within error bars). Thus, we conclude that the substrate influence on the reported  $E_r$  values is negligible.

Determination of the stress in the textured coatings was carried out by determining the curvature of the substrate by performing rocking curve measurements of the (400) reflection of the single crystal Si-substrate.<sup>38</sup> A PANalytical Empyrean diffractometer was operated in point focus and equipped with 3-bounce Ge (200) monochromators as the primary and secondary optics, respectively. Rocking curve measurements were performed at nine different locations along a straight line on the sample, oriented perpendicularly to the rocking rotation axis. The substrate-curvature radius,  $R$ , is then determined as the slope of a plot of the measurement positions,  $x$ , versus the peak position of the rocking curve,  $\omega$ ,

$$R = \frac{\Delta x}{\Delta \omega}. \quad (1)$$

The intrinsic radius of the bare substrate is much greater than the radius induced by the coatings; therefore, the influences of intrinsic substrate radius are neglected. The stress of the coating is then calculated by the Stoney equation,<sup>39</sup>

$$\sigma = \frac{1}{6} \frac{E_s}{1 - \nu_s} \frac{h_s^2}{h_f R}, \quad (2)$$

where  $\sigma$  is the residual stress, and  $E_s$  and  $\nu_s$  are the elastic modulus and Poisson's ratio of the substrate, respectively. For Si (001), the modulus  $E_s = 165$  GPa and  $\nu_s = 0.22$  at room temperature.<sup>40</sup>  $h_s = 430\text{ }\mu\text{m}$  and  $h_f = 1332 \div 1663$  nm (Table II) are the thickness of the substrate and coating, respectively.

Consequently, the bending moment from the coating and resultant flexure stress can be neglected.<sup>41</sup>

**TABLE II.** Thickness, the multilayer period ( $\Lambda$ ), and the chemical compositions of the TiVNbMoWN films.

$V_s$ , V	Thickness (nm)		Elemental composition (at. %)							
	Full	$\Lambda$	Ti	V	Nb	Mo	W	Ar	O	N
60	1332	2.16	$3.3 \pm 0.1$	$12.8 \pm 0.2$	$2.4 \pm 0.2$	$18.5 \pm 0.2$	$17.1 \pm 0.2$	$0.8 \pm 0.1$	$1.1 \pm 0.1$	$44.1 \pm 0.4$
300	1663	1.92	$3.2 \pm 0.1$	$12.1 \pm 0.1$	$2.5 \pm 0.1$	$19.0 \pm 0.1$	$18.7 \pm 0.1$	$1.4 \pm 0.1$	$0.4 \pm 0.1$	$42.8 \pm 0.6$
600	1570	1.82	$2.9 \pm 0.2$	$10.3 \pm 0.1$	$2.2 \pm 0.2$	$17.6 \pm 0.1$	$20.1 \pm 0.2$	$4.8 \pm 0.1$	$0.4 \pm 0.1$	$41.8 \pm 0.6$

16 November 2023 15:31:20

### III. RESULTS

#### A. Chemical composition

The volume-averaged chemical compositions of the TiVNbMoWN films determined by EDS and ERDA are presented in Table II. The compositions of metals in the grown films are  $\text{Ti}_6\text{V}_{24}\text{Nb}_4\text{Mo}_{34}\text{W}_{32}\text{N}$ ,  $\text{Ti}_6\text{V}_{22}\text{Nb}_4\text{Mo}_{34}\text{W}_{34}\text{N}$ , and  $\text{Ti}_5\text{V}_{19}\text{Nb}_4\text{Mo}_{33}\text{W}_{38}\text{N}$  for  $V_s = 60$ , 300, and 600 V, respectively. With increasing substrate bias amplitude, the W metal fraction increases from 0.32 to 0.38, the Mo and Nb fractions do not change, while the V and Ti fractions decrease from 0.24 to 0.19 and from 0.06 to 0.05, respectively. These variations can be explained by the preferential resputtering of lighter components (V and Ti) by heavy W ions, an effect that increases with increasing  $W^+$  incident energy. Given that the configuration entropy parameter of the metal sublattice is  $\sim 1.36 R$ , all films can be classified into the family of high-entropy sublattice nitrides.<sup>42</sup>

According to the results of ToF-ERDA analysis, the nitrogen/metal ratio in TiVNbMoWN films decreases with increasing

substrate bias amplitude from  $C_N/C_{Me} = 0.82$  with  $V_s = 60$  V to 0.77 and 0.79 with  $V_s = 300$  and 600 V, respectively. The oxygen concentration decreases from  $1.1 \pm 0.1$  at. % at  $V_s = 60$  V to  $0.4 \pm 0.1$  at. % at higher  $V_s$  values. This trend is indicative of the increasing film density upon the increase in  $V_s$ , which obstructs O diffusion along grain boundaries.<sup>43</sup> As all films are deposited at the same background pressure, oxygen adsorbed during growth cannot explain these differences, which are, thus, assigned to inward O diffusion upon air exposure. The Ar concentration increases from  $0.8 \pm 0.1$  at. % with  $V_s = 60$  V to  $1.4 \pm 0.1$  and  $4.8 \pm 0.1$  at. % with  $V_s = 300$  and 600 V, respectively.

#### B. X-ray diffractometry

The wide range  $\theta$ - $2\theta$  XRD scans obtained from TiVNbMoWN films grown with  $V_s = 60$ , 300, and 600 V are shown in Fig. 2(a). All films are single phase with a fcc B1 NaCl crystal structure, as evidenced by the presence of (111), (200), (311), (222), and (400) reflections. No preferred orientation is observed

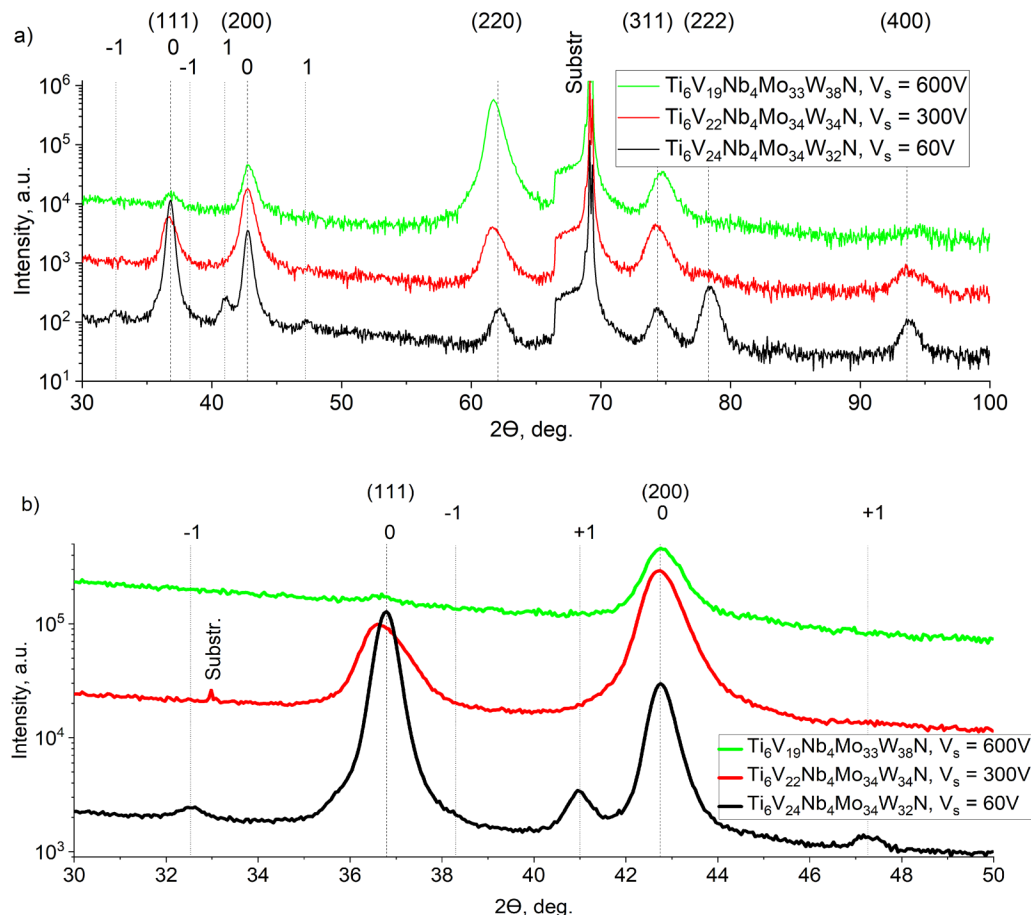


**FIG. 2.** X-ray diffractograms recorded from TiVNbMoWN films grown on Si substrates as a function of substrate bias amplitude: (a)  $2\theta$  from  $30^\circ$  to  $100^\circ$ ; (b)  $2\theta$  from  $30^\circ$  to  $50^\circ$ .

16 November 2023 15:31:20



for films grown with  $V_s = 60$  and 300 V. XRD shows a slight shift in the preferred orientation toward 002 for films grown with  $V_s = 600$  V.

The lattice parameter determined from Bragg's formula is 0.4229 nm for films deposited with  $V_s = 60$  V and  $V_s = 300$  V, and decreases slightly by increasing the bias amplitude to 0.4223 nm for films grown with  $V_s = 600$  V. The crystal size, determined by the Williamson–Hall method, decreases with an increase in the substrate bias amplitude from 28.1 nm with  $V_s = 60$  V to 19.2 and 17.3 nm with  $V_s = 300$  and 600 V, respectively. This effect stems from an increased renucleation rate due to irradiation with heavy  $W^+$  ions, which scales with increasing average energy and momentum of incident ions.<sup>43,44</sup>

In the diffractogram from the TiVNbMoWN film grown with  $V_s = 60$  V, satellite peaks are observed around 111 and 200 reflections [see Fig. 2(b)], revealing compositional modulation. Markedly, these peaks are absent for films grown with  $V_s = 300$  and 600 V. The multi-layer period ( $\Lambda$ ) can be calculated from the following equation:<sup>45</sup>

$$\Lambda = \frac{\lambda_{\text{CuK}\alpha}}{2(\sin\theta_n - \sin\theta_{n-1})}, \quad (3)$$

where  $\lambda_{\text{CuK}\alpha} = 0.15405$  nm is the wavelength of the incident x-ray and  $\theta_n$  is the diffraction angle corresponding to the  $n_{\text{th}}$ -order peak in the rocking curve. For the coating grown with  $V_s = 60$  V,  $L = 2.09$  nm for (111) satellites and 1.97 nm for (200) satellites.

### C. Film microstructure

SEM micrographs of fractured cross sections from TiVNbMoWN films deposited with  $V_s$  varying from 60, 300, and 600 V are presented in Figs. 3(a)–3(c). Based on the cross-sectional images, there is no apparent porosity in any of the films. In the

case of  $V_s = 60$  V, the film has well-defined columns with a width that increases as a function of distance from the substrate. With  $V_s = 300$  V, the columnar structure is less defined and eventually disappears in films grown with the highest bias amplitude of 600 V. One effect is responsible for that—the disruption of the local epitaxial growth on individual columns due to radiation damage as a result of high energy W ion bombardment.<sup>46,47</sup>

The film deposition rate determined from SEM images is 6.48 nm/min with  $V_s = 60$  V and decreases to 5.78 and 5.46 nm/min with  $V_s = 300$  and 600 V, respectively.<sup>28,48,49</sup> Taking into account that the substrate holder rotates at a speed of 3.08 rpm, the thickness deposited during one complete revolution is 2.16 nm with  $V_s = 60$  V and decreases to 1.92 and 1.82 nm with  $V_s = 300$  and 600 V, respectively.

The results of TEM analysis are shown in Fig. 4. For TiVNbMoWN films grown with the substrate bias amplitude of 60 V, TEM and STEM images [cf., Figs. 4(a) and 4(c)] show the formation of a layered structure with a periodicity of  $\sim 2.0$  nm. With  $V_s = 300$  V, the layers are not so well defined in TEM images but remain well-resolved in STEM [cf., Figs. 4(d) and 4(f)]. The periodicity extracted from TEM and STEM is  $\sim 2.0$  nm. At a bias voltage of 600 V, the layering disappears in both TEM and STEM [see Figs. 4(g) and 4(i)], revealing the formation of compositionally uniform HESN films.

The SAED patterns from all TiVNbMoWN films [Figs. 4(b), 4(e), and 4(h)] consist of mixed cubic 111, 002, 022, 113, 222, 004, 133, and 024 diffraction rings. Films are nanocrystalline as they do not show any particular preferred crystallographic orientation.

### D. Mechanical properties

The nanoindentation hardness  $H$  for TiVNbMoWN films grown with  $V_s = 60$  V is  $23.7 \pm 0.5$  GPa and increases to  $28.9 \pm 0.4$  and  $29.9 \pm 0.8$  GPa for layers deposited with  $V_s = 300$  and 600 V, respectively. The reduced Young modulus decreases with an

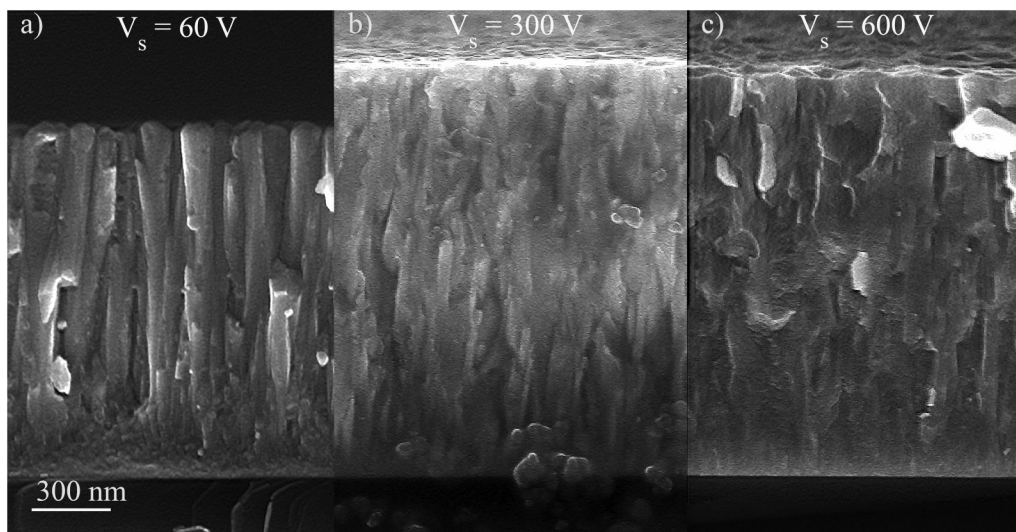


**FIG. 3.** Cross-sectional SEM images of thin films deposited on Si substrates with the amplitude of the synchronized substrate bias of TiVNbMoWN films:  $V_s = 60$  (a), 300 (b), 600 V (c).

16 November 2023 15:31:20

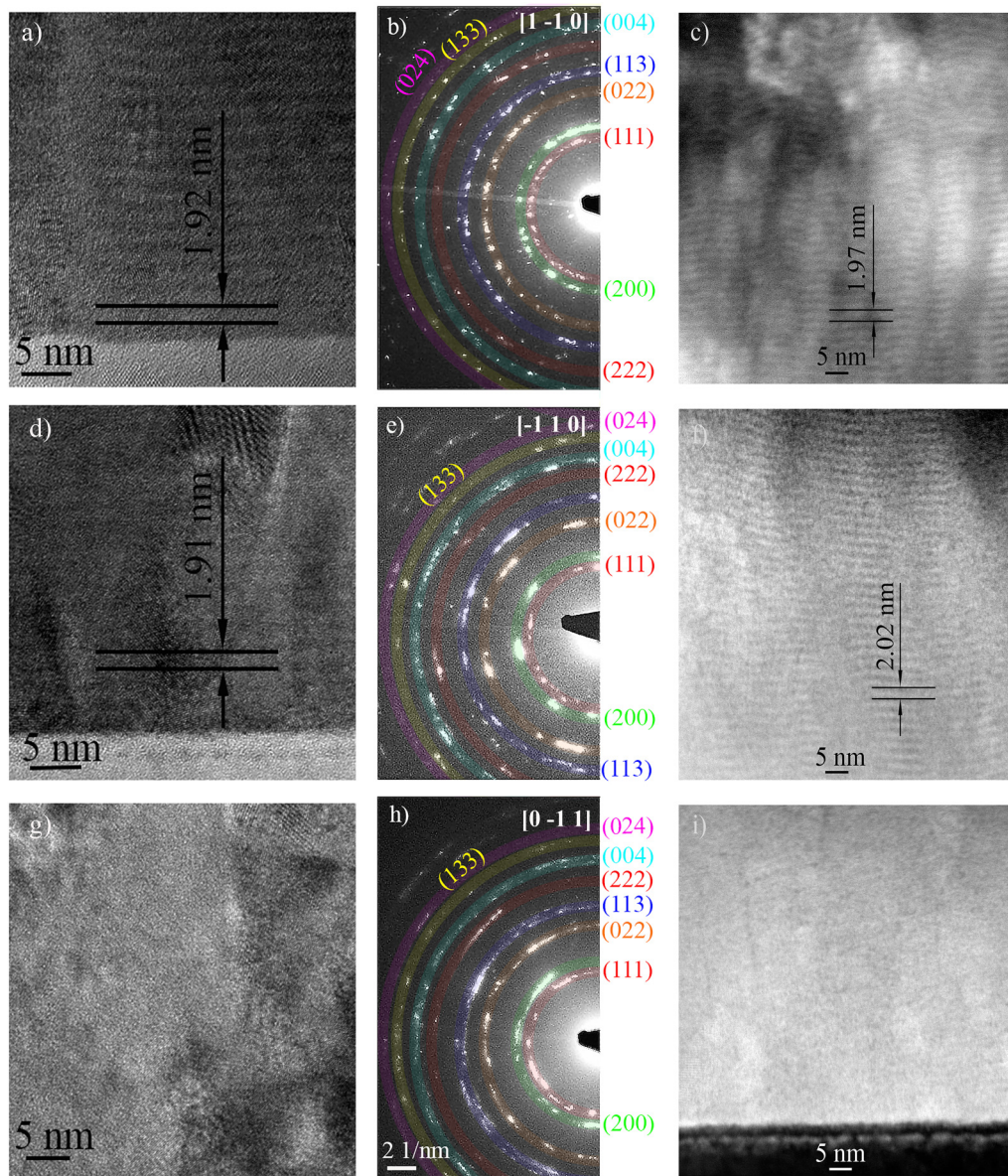


**FIG. 4.** Cross-sectional TEM images (a), (d), and (g); SAED (b), (e), and (h) and STEM (c), (f), and (i) images for films grown on Si substrates:  $V_s = 60$  (a)–(c), 300 (d)–(f), and 600 V (g)–(i).

increase in  $V_s$  from  $311.7 \pm 5.7$  with  $V_s = 60$  V to  $296.0 \pm 3.6$  GPa with  $V_s = 300$  V and  $275.1 \pm 5.1$  GPa with  $V_s = 600$  V. Accordingly, the resistance to plastic deformation characterized by  $H^3/Er^2$  (Refs. 50 and 51) is  $0.14 \pm 0.01$  GPa for  $V_s = 60$  V,  $0.28 \pm 0.01$  GPa for  $V_s = 300$  V, and  $0.36 \pm 0.02$  GPa for  $V_s = 600$  V.

The residual stress  $\sigma$  is  $-1.1 \pm 0.1$ ,  $-3.2 \pm 0.1$ , and  $-4.3 \pm 0.2$  GPa for TiVNbMoWN films grown with  $V_s = 60$ , 300, and 600 V, respectively.

#### IV. DISCUSSION

The results presented in the previous section demonstrate that the amplitude of the substrate bias applied synchronously with the HiPIMS pulse during the time the substrate faces the HiPIMS target has a determining effect on the compositional homogeneity of TiVNbMoWN films and resulting mechanical properties. TEM and STEM images reveal that a multilayered structure is not



significantly affected for films deposited with a relatively low  $V_s$  of 60 V (corresponding to the  $W^+$  ion energy  $E_{W^+} = 80$  eV), while compositionally uniform HESN films are obtained with  $V_s = 600$  V ( $E_{W^+} = 620$  eV).

To understand these effects, we need to consider that in magnetron sputtering, the average energy of ions impinging onto the film surface is given by

$$E_i = E_{io} + ne(V_s - V_p), \quad (4)$$

where  $E_{io}$  is the average energy of ions entering the anode sheath (corresponding to the sputter energy),  $n$  is the ion charge state,  $V_s$  is the amplitude of the negative bias voltage applied to the substrate, and  $V_p$  is the plasma potential.<sup>52</sup> We assume the collisionless transport of the metal ions in the accelerating bias sheath, which is reasonable given the mTorr-pressure range and sputtering plasma.<sup>53</sup> Under the applied process conditions,  $E_{io} \sim 30$  eV for  $W^+$  ions,<sup>55</sup> while  $V_p$  is in the range 5–10 V.<sup>32</sup> Thus,  $E_i \approx eV_s$  as the contribution of doubly ionized  $W^{2+}$  ions does not exceed a few %.<sup>35</sup>

It is intuitively understood that for the complete compositional mixing, the range of  $W^+$  induced collision cascades has to be comparable to the thickness of the layer deposited in between two consecutive exposures to  $W^+$  flux from the HiPIMS source.<sup>27</sup> The thickness of the latter layer is not directly accessible as it would require depositing films from DCMS sources only (with the HiPIMS cathode off) while applying synchronized substrate bias. As that is not possible to realize in the equipment used for these experiments, we base the discussion below on the multilayer thickness (which can be, in fact, considered the upper limit for the thickness of the material deposited from DCMS sources) estimated from (I) the total film thickness assessed by SEM divided by the number of substrate revolutions ( $\Lambda$ ), (II) positions of XRD satellite peaks, and (III) TEM/STEM images. For coatings grown with  $V_s = 60$  V, the corresponding values are  $\sim 2.2$  (I),  $\sim 2.0$  (II), and  $\sim 2.0$  nm (III), respectively. The difference in values obtained by different methods is attributed to experimental errors. Thus, the average layer thickness is  $2.1 \pm 0.1$  nm. For coatings obtained at  $V_s = 300$  V, the values of the layer thickness are  $\sim 1.9$  (I) and  $\sim 2.0$  nm (III). Therefore, the average layer thickness is  $2.0 \pm 0.1$  nm. In the case of  $V_s = 600$  V, no layered structure is observed by any of the methods, but the thickness of the layer deposited in one revolution can be estimated to be  $\sim 1.8$  nm (I).

For estimates of the depth of collision cascades, we use Monte Carlo TRIM simulations of  $W^+$  ions impinging onto a multilayered MoN/NbN/TiN/VN/ $W_2N$ /MoN/TiVNbMoWN structure,<sup>49</sup> reflecting the sequence, in which targets are arranged in the deposition chamber (cf., Fig. 1). Due to the limitations of TRIM at low energies, the presented discussion is based on qualitative comparisons.<sup>54</sup> In the simulation, the  $W^+$  ion flux is directed along the surface normal with constant ion energy of 80, 320, and 620 eV corresponding to  $V_s = 60$ , 300, and 600 V, respectively. The thickness of each layer used for modeling (Table III) is calculated based on the film composition obtained from the EDS analysis. We assume that half of the atoms leaving the W target is ionized and contributes to intermixing, while<sup>55</sup> the other half is deposited as neutrals on the surface of the growing layer.

TABLE III. Parameters for TRIM modeling.

Layer	Thickness (nm)			Density (g/cm <sup>3</sup> )
	$V_s = 60$ V	$V_s = 300$ V	$V_s = 600$ V	
VN	0.52	0.42	0.35	6.13
MoN	0.74	0.66	0.60	9.46
$W_2N$	0.34	0.33	0.35	17.8
NbN	0.10	0.09	0.08	8.47
TiN	0.13	0.11	0.10	5.4

The first clear effect of an increasing substrate bias amplitude is that the  $W^+$  implantation depth increases from 1.8 nm with  $V_s = 60$  V to 3.2 nm with  $V_s = 600$  V. The ion-induced mixing is also affected, as revealed by details of recoil distributions plotted in Fig. 5. With  $V_s = 60$  V ( $E_{W^+} = 80$  eV), the near-surface intermixing zone, defined by the average depth of collision cascades, corresponds to the effective depth of Mo recoils (the number of other recoils is negligibly small) and amounts to  $\sim 1.8$  nm. The latter is lower than the layer thickness grown during one full substrate rotation,  $2.02 \pm 0.10$  nm; thus, the  $W^+$  ion energy of 80 eV is insufficient to affect the entire layer deposited between two consecutive substrate exposures to the HiPIMS cathode. As a consequence of that, the films grow with a periodic structure [Figs. 4(a) and 4(c)], with well-defined layers giving rise to XRD satellite peaks around (111) and (200) reflections [cf., Fig. 2(b)].

With  $V_s = 300$  V ( $E_{W^+} = 320$  eV), the  $W^+$  implantation range increases to 2.5 nm [cf., Fig. 5(b)], which exceeds the average thickness of the layer deposited during one full substrate rotation,  $2.0 \pm 0.1$  nm, as calculated based on SEM, TEM, and STEM analyses [Figs. 4(b) and 4(d)]. The effective W and Mo recoil ranges are  $\sim 2.4$  nm, while the corresponding values for Ti, Nb, V, and N recoils are  $\sim 1.9$ ,  $\sim 2.0$ ,  $\sim 2.2$ , and  $\sim 2.1$  nm, respectively. This naturally causes the blurring of layer boundaries in the TEM image [Fig. 4(d)]. The smearing of the interfaces between the layers results in the disappearance of the satellite peaks [due to the loss of the square wave modulation, cf., Fig. 2(b)] although the compositional modulation is visible in STEM images [Fig. 4(f)].

With  $V_s = 600$  V ( $E_{W^+} = 620$  eV), the near-surface intermixing zone extends to 3.2 nm [Fig. 5(c)], which is clearly more than the thickness of the layer deposited during one substrate rotation (1.8 nm): the W, Mo, N, V, Ti, and Nb recoil ranges are  $\sim 3.2$ ,  $\sim 3.2$ ,  $\sim 2.9$ ,  $\sim 2.8$ ,  $\sim 2.6$ , and  $\sim 2.7$  nm, respectively. Under such conditions, the  $W^+$  energy is sufficient to cause complete intermixing of the DCMS-deposited material such that compositionally uniform HESN films are obtained, as evidenced by the fact that no periodic structures are observed in corresponding TEM and STEM images [Figs. 4(i) and 4(g)].

Suppression of crystallite growth as a result of ion bombardment contributes to an increase in the hardness in accordance with the Hall–Petch relation:<sup>55,56</sup> with the decrease in the crystallite size from 28.1 to 17.3 nm, the hardness increases from  $23.7 \pm 0.5$  to  $29.9 \pm 0.8$  GPa with  $V_s = 60$  V and 600 V, respectively. In addition to compressive stresses (see below), this mechanism has a major impact on the hardness evolution.

16 November 2023 15:31:20



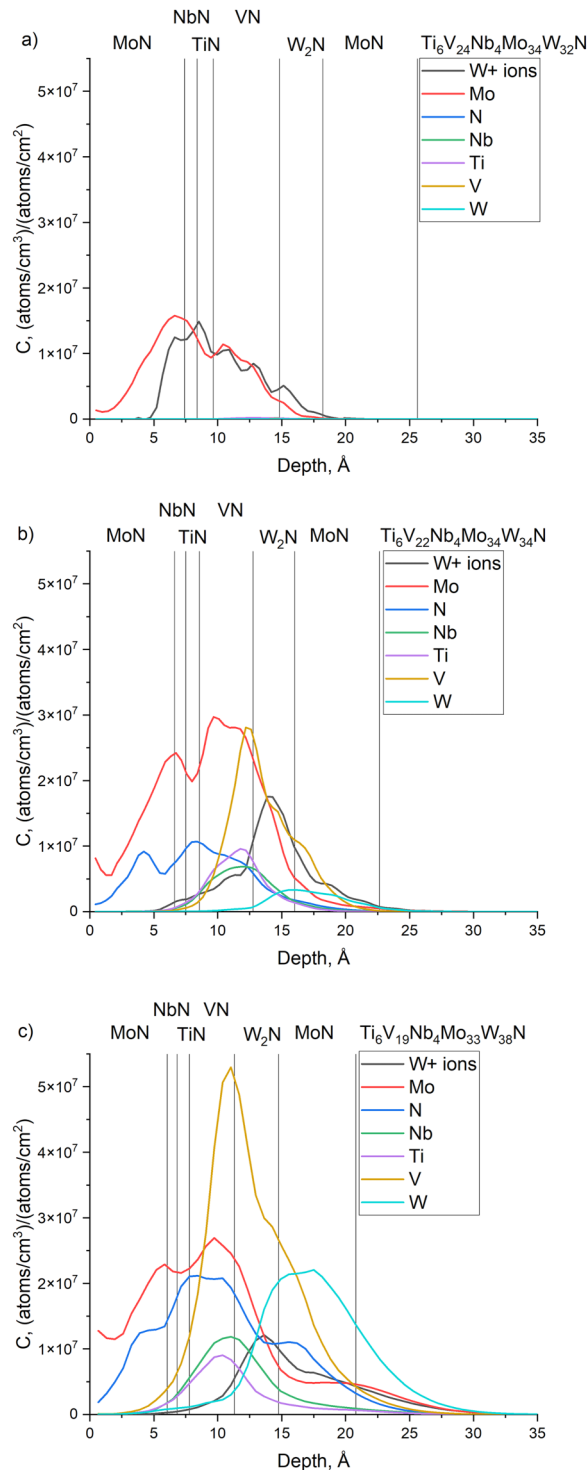


**FIG. 5.** TRIM simulations of the effects of 80 (a), 320 (b), and 620 eV (c)  $W^+$  ion bombardment of MoN/NbN/TiN/VN/ $W_2N$ /MoN/Ti/VNbMoWN films. Plots show the distributions of primary recoils and implanted  $W^+$  ions.

In the experimental setup used here,  $W^+$  ion irradiation is active only when the substrate is in front of the HiPIMS cathode, while for the rest of deposition time, the growing film surface is exposed to gas ion irradiation. As a consequence of that, an increase in  $V_s$  from 60 to 600 V causes an increase in the average energy of  $Ar^+$  ions incident at the growing film surface. This results in an increase in the trapped Ar concentration from  $0.8 \pm 0.1$  at. % with  $V_s = 60$  V to  $4.8 \pm 0.1$  at. % with  $V_s = 600$  V, which is the main reason for the increase in the compressive stress from  $-1.1 \pm 0.1$  to  $-4.3 \pm 0.2$  GPa. The latter is (to some extent) responsible for the observed increase in the film hardness.

It is well-known that an increase in the compressive stress state leads to higher elastic modulus values.<sup>57</sup> However, for TiVNbMoWN films,  $E_r$  decreases with increasing compressive stress. This is explained by the structural modification as the film transforms from the multilayer to a compositionally uniform structure upon increasing the substrate bias amplitude. It has been demonstrated (see, e.g., Ref. 58) that multilayer coatings tend to have a higher reduced Young's modulus. Thus, we assign the observed decrease in the reduced Young's modulus to the structural modification. The latter effect seems to dominate over the potential increase in  $E_r$  due to a higher compressive stress state.

Detrimental effects of  $Ar^+$  ion irradiation could be potentially avoided by using a higher substrate rotation speed, which would allow to lower the bias amplitude values required to ensure a homogeneous HEA composition. Our simulations (not shown) indicate that  $V_s = 300$  V would suffice for 4 rpm rotational speed, which is close to the industrial practice. Another solution would be to apply the second-order bias synchronization such that the substrate would be electrically floating while facing DCMS magnetrons.

Resputtering also is an important aspect that needs to be considered if HESN films with specific compositions are desired. In such a case, the loss of lighter elements can be easily compensated for by increasing the power on the corresponding DCMS cathode.

## V. CONCLUSIONS

An original method for the growth of compositionally uniform high-entropy alloy thin films is presented. The concept relies on using several elemental targets mounted on separate magnetrons in a multicathode sputtering system with rotating substrates such that the composition of the films can easily be controlled by varying the power to each magnetron. To avoid substrate-rotation-induced compositional modulations over the film thickness, the growing film surface is periodically exposed to the flux of  $W^+$  ions provided by the W target operating in the HiPIMS mode. This leads to the dynamic recoil mixing of the film-forming components in the near-surface atomic layers, which allows to suppress the multilayer formation. The thickness of the ion mixing zone is determined by the metal ion energy and momentum transfer, which are both controlled by varying the amplitude of the negative substrate bias pulses  $V_s$  that are synchronized to  $W^+$  ion fluxes during the time period when the substrate is facing the HiPIMS target. The method is cheaper than the traditional approach that relies on the use of compound targets and allows for large flexibility in adjusting the HEA composition.

16 November 2023 15:31:20

For demonstration of the basic principle, TiVNbMoWN films are grown using Ti, V, Nb, and Mo targets mounted on DCMS magnetrons, while the W target operated by HiPIMS provides a source of heavy ions to ensure sufficient intermixing in the topmost atomic layers. It is shown that by increasing  $V_s$  from 60 to 600 V, the multilayer structure, commonly obtained during deposition with rotating substrates, evolves toward a compositionally uniform single-phase film. The critical parameter that controls the growth is the relation between the thickness of the layer deposited during one complete substrate rotation and the depth of  $W^+$ -induced collision cascades. Once the latter exceeds the former, compositionally uniform high-entropy sublattice nitride films are obtained.

## ACKNOWLEDGMENTS

The authors most gratefully acknowledge the financial support of the SSF via Grant No. UKR22-0031, Swedish Research Council VR (Grant No. 2018-03957), the Swedish Energy Agency under Project No. 51201-51201, the Åfors Foundation under Grant No. 22-4, the Knut and Alice Wallenberg (KAW) Foundation Scholar under Grant No. KAW2019.0290, the Olle Enqvist foundation under Grant No. 222-0053, and the Carl Tryggers Stiftelse under Contract No. CTS 20:150. Support from the Swedish Research Council VR-RFI (2019\_00191) for the Accelerator based ion-technological center for the Tandem Accelerator Laboratory at Uppsala University is acknowledged. This work was partially supported by the Wallenberg Initiative Materials Science for Sustainability (WISE) funded by the Knut and Alice Wallenberg Foundation. The authors also thank KAW for the support of the electron microscopy laboratory in Linköping and the Swedish Research Council and SSF for access to ARTEMIS, the Swedish National Infrastructure in Advanced Electron Microscopy (2021-00171 and RIF21-0026). B.W. is grateful to the Polish National Agency for Academic Exchange for the support upon the NAWA Bekker No. BPN/BEK/2021/1/00366/U/00001 project.

## AUTHOR DECLARATIONS

### Conflict of Interest

The authors have no conflicts to disclose.

### Author Contributions

**Vladyslav Rogoz:** Conceptualization (equal); Formal analysis (equal); Investigation (equal); Methodology (equal); Visualization (lead); Writing – original draft (lead). **Oleksandr Pshyk:** Investigation (equal); Writing – review & editing (equal). **Bartosz Wicher:** Investigation (equal); Writing – review & editing (equal). **Justinas Palisaitis:** Investigation (equal); Writing – review & editing (equal). **Jun Lu:** Investigation (equal); Writing – review & editing (equal). **Daniel Primetzhof:** Formal analysis (equal); Investigation (equal); Writing – review & editing (equal). **Ivan Petrov:** Conceptualization (equal); Data curation (equal); Writing – review & editing (equal). **Lars Hultman:** Conceptualization (equal); Data curation (equal); Supervision (equal); Writing – review & editing (equal). **Grzegorz Greczynski:** Conceptualization

(equal); Methodology (equal); Project administration (equal); Supervision (equal); Writing – review & editing (equal).

## DATA AVAILABILITY

The data that support the findings of this study are available from the corresponding author upon reasonable request.

## REFERENCES

- <sup>1</sup>K. Bobzin, *CIRP J. Manuf. Sci. Technol.* **18**, 1 (2017).
- <sup>2</sup>N. Schalk, M. Tkadletz, and C. Mitterer, *Surf. Coat. Technol.* **429**, 127949 (2022).
- <sup>3</sup>I. Kraljinić *et al.*, *Surf. Coat. Technol.* **304**, 134 (2016).
- <sup>4</sup>A. Pogrebnjak, V. Rogoz, V. Ivashchenko, O. Bondar, V. Shevchenko, S. Jurga, and E. Coy, *J. Alloys Compd.* **718**, 260 (2017).
- <sup>5</sup>O. V. Maksakova *et al.*, *J. Alloys Compd.* **831**, 154808 (2020).
- <sup>6</sup>A. D. Pogrebnjak, V. M. Rogoz, O. V. Bondar, N. K. Erdybaeva, and S. V. Plotnikov, *Prot. Met. Phys. Chem. Surf.* **52**, 802 (2016).
- <sup>7</sup>B. Cantor, *Prog. Mater. Sci.* **120**, 100754 (2021).
- <sup>8</sup>X. You, J. Song, P. Lin, X. Zhang, Y. Su, H. Wang, Y. Zhang, and L. Hu, *Tribol. Int.* **175**, 107801 (2022).
- <sup>9</sup>A. Motallebzadeh, *Surf. Coat. Technol.* **448**, 128918 (2022).
- <sup>10</sup>X. Liu, D. Hua, W. Wang, Q. Zhou, S. Li, J. Shi, Y. He, and H. Wang, *J. Alloys Compd.* **920**, 166058 (2022).
- <sup>11</sup>Y. Tian, W. Zhou, M. Wu, H. Luo, Q. Tan, G. Zhu, A. Dong, D. Shu, and B. Sun, *J. Alloys Compd.* **915**, 165324 (2022).
- <sup>12</sup>J. W. Yeh, *Ann. Chim. Sci. Matér.* **31**, 633 (2006).
- <sup>13</sup>Y. Tang, R. Wang, B. Xiao, Z. Zhang, S. Li, J. Qiao, S. Bai, Y. Zhang, and P. K. Liaw, *Prog. Mater. Sci.* **135**, 101090 (2023).
- <sup>14</sup>D. Qiao, H. Liang, S. Wu, J. He, Z. Cao, Y. Lu, and T. Li, *Mater. Charact.* **178**, 111287 (2021).
- <sup>15</sup>H. Kim, S. Nam, A. Roh, M. Son, M. H. Ham, J. H. Kim, and H. Choi, *Int. J. Refract. Met. Hard Mater.* **80**, 286 (2019).
- <sup>16</sup>S. Zhao *et al.*, *Surf. Coat. Technol.* **417**, 127228 (2021).
- <sup>17</sup>P. Hruška *et al.*, *J. Alloys Compd.* **869**, 157978 (2021).
- <sup>18</sup>B. Song, Y. Li, Z. Cong, Y. Li, Z. Song, and J. Chen, *J. Alloys Compd.* **797**, 1025 (2019).
- <sup>19</sup>C. Zhu, L. Xu, M. Liu, M. Guo, and S. Wei, *J. Mater. Res. Technol.* **24**, 7832 (2023).
- <sup>20</sup>M. Y. He, Y. F. Shen, N. Jia, and P. K. Liaw, *Appl. Mater. Today* **25**, 101162 (2021).
- <sup>21</sup>J. Wang, S. Kuang, X. Yu, L. Wang, and W. Huang, *Surf. Coat. Technol.* **403**, 126374 (2020).
- <sup>22</sup>Y. Zhao, X. Zhang, H. Quan, Y. Chen, S. Wang, and S. Zhang, *J. Alloys Compd.* **895**, 162709 (2022).
- <sup>23</sup>S. Oladijo, F. M. Mwema, T. C. Jen, K. Ronoh, D. Sobola, and E. T. Akinlabi, *Mater. Today Commun.* **33**, 104523 (2022).
- <sup>24</sup>X. Zhang, V. Pelenovich, Y. Liu, X. Ke, J. Zhang, B. Yang, G. Ma, M. Li, and X. Wang, *Vacuum* **195**, 110710 (2022).
- <sup>25</sup>Y. Xu, G. Li, G. Li, F. Gao, and Y. Xia, *Appl. Surf. Sci.* **564**, 150417 (2021).
- <sup>26</sup>A. V. Pshyk, A. Vasylenko, B. Bakhit, L. Hultman, P. Schweizer, T. E. J. Edwards, J. Michler, and G. Greczynski, *Mater. Des.* **219**, 110798 (2022).
- <sup>27</sup>G. Greczynski, J. Lu, S. Bolz, W. Kölker, C. Schiffrers, O. Lemmer, I. Petrov, J. E. Greene, and L. Hultman, *J. Vac. Sci. Technol. A* **32**, 041515 (2014).
- <sup>28</sup>X. Li, B. Bakhit, M. P. J. Jösaar, L. Hultman, I. Petrov, and G. Greczynski, *Surf. Coat. Technol.* **415**, 127120 (2021).
- <sup>29</sup>G. Greczynski *et al.*, *J. Vac. Sci. Technol. A* **30**, 061504 (2012).
- <sup>30</sup>J. F. Ziegler, M. D. Ziegler, and J. P. Biersack, *Nucl. Instrum. Methods Phys. Res., Sect. B* **268**, 1818 (2010).
- <sup>31</sup>G. Greczynski, S. Mráz, L. Hultman, and J. M. Schneider, *Appl. Phys. Lett.* **108**, 041603 (2016).

16 November 2023 15:31:20

- <sup>32</sup>G. Greczynski, I. Petrov, J. E. Greene, and L. Hultman, *J. Vac. Sci. Technol. A* **37**, 060801 (2019).
- <sup>33</sup>V. Buranich, V. Rogoz, B. Postolnyi, and A. Pogrebnyak, in *2020 IEEE 10th International Conference Nanomaterials: Applications & Properties (NAP)* (IEEE, 2020).
- <sup>34</sup>B. Postolnyi, V. Buranich, K. Smyrnova, J. P. Araújo, L. Rebouta, A. Pogrebnyak, and V. Rogoz, *IOP Conf. Ser.: Mater. Sci. Eng.* **1024**, 012009 (2021).
- <sup>35</sup>G. Greczynski, I. Zhirkov, I. Petrov, J. E. Greene, and J. Rosen, *J. Vac. Sci. Technol. A* **36**, 020602 (2018).
- <sup>36</sup>P. Ström and D. Primetzhofer, *J. Instrum.* **17**, P04011 (2022).
- <sup>37</sup>W. C. Oliver and G. M. Pharr, *J. Mater. Res.* **19**, 3 (2004).
- <sup>38</sup>J. Keckes, E. Eiper, K. J. Martinschitz, H. Köstenbauer, R. Daniel, and C. Mitterer, *Rev. Sci. Instrum.* **78**, 036103 (2007).
- <sup>39</sup>P. H. Mayrhofer and C. Mitterer, *Surf. Coat. Technol.* **133-134**, 131 (2000).
- <sup>40</sup>L. B. Freund and S. Suresh, *Thin Film Materials Stress, Defect Formation and Surface Evolution* (Cambridge University, Cambridge, 2004).
- <sup>41</sup>H. Windischmann and K. J. Gray, *Diamond Relat. Mater.* **4**, 837 (1995).
- <sup>42</sup>D. B. Miracle and O. N. Senkov, *Acta Mater.* **122**, 448 (2017).
- <sup>43</sup>G. Greczynski *et al.*, *Thin Solid Films* **556**, 87 (2014).
- <sup>44</sup>G. Greczynski, J. Lu, O. Tengstrand, I. Petrov, J. E. Greene, and L. Hultman, *Scr. Mater.* **122**, 40 (2016).
- <sup>45</sup>D. K. Bowen and Tanner K. Brian, *High Resolution X-Ray Diffractometry and Topography* (Taylor & Francis Ltd, London, 1998).
- <sup>46</sup>I. Petrov, P. B. Barna, L. Hultman, and J. E. Greene, *J. Vac. Sci. Technol. A* **21**, S117 (2003).
- <sup>47</sup>I. Petrov, L. Hultman, U. Helmersson, J.-E. Sundgren, and J. E. Greene, *Thin Solid Films* **169**, 299 (1989).
- <sup>48</sup>X. Li, B. Bakhit, M. P. Johansson Jösaar, I. Petrov, L. Hultman, and G. Greczynski, *Surf. Coat. Technol.* **424**, 127639 (2021).
- <sup>49</sup>A. V. Pshyk, I. Petrov, B. Bakhit, J. Lu, L. Hultman, and G. Greczynski, *Mater. Des.* **227**, 111753 (2023).
- <sup>50</sup>T. Y. Tsui, G. M. Pharr, W. C. Oliver, C. S. Bhatia, S. Anderst, A. Anderst, and I. G. Brown, *MRS Proc.* **383**, 447 (1995).
- <sup>51</sup>J. Musil, F. Kunc, H. Zeman, and H. Poláková, *Surf. Coat. Technol.* **154**, 304 (2002).
- <sup>52</sup>I. Petrov, F. Adibi, J. E. Greene, L. Hultman, and J. E. Sundgren, *Appl. Phys. Lett.* **63**, 36 (1993).
- <sup>53</sup>M. A. Lieberman and A. J. Lichtenberg, *Principles of Plasma Discharges and Materials Processing*, Second Edition (John Wiley & Sons, Inc., Hoboken, NJ, 2005), pp. 1–22.
- <sup>54</sup>G. Hobler and G. Betz, *Nucl. Instrum. Methods Phys. Res., Sect. B* **180**, 203 (2001).
- <sup>55</sup>E. O. Hall, *Proc. Phys. Soc., Sect. B* **64**, 747 (1951).
- <sup>56</sup>N. Petch, *J. Iron Steel Inst.* **174**, 25 (1953).
- <sup>57</sup>D. Music *et al.*, *J. Appl. Phys.* **121**, 215108 (2017).
- <sup>58</sup>M. I. Yousaf, V. O. Pelenovich, B. Yang, C. S. Liu, and D. J. Fu, *Surf. Coat. Technol.* **282**, 94 (2015).